

1

2 **The Aerosol Module in the Community Radiative Transfer Model** 3 **(v2.2 and v2.3): accounting for aerosol transmittance effects on the** 4 **radiance observation operator**

5 Cheng-Hsuan (Sarah) Lu^{1,2}, Quanhua Liu³, Shih-Wei Wei^{1,2}, Benjamin T. Johnson⁴, Cheng Dang¹,
6 Patrick G. Stegmann⁴, Dustin Grogan², Guoqing Ge^{5,6}, Ming Hu⁶, and Michael Lueken^{7,8}

7
8 ¹Joint Center for Satellite Data Assimilation, Boulder, CO, USA

9 ²Atmospheric Sciences Research Center, University at Albany, Albany, NY, USA

10 ³Center for Satellite Applications and Research, NOAA/NESDIS, College Park, MD, USA

11 ⁴Joint Center for Satellite Data Assimilation, College Park, MD, USA

12 ⁵Cooperative Institute for Research in Environmental Sciences, CU Boulder, CO, USA

13 ⁶Global System Laboratory, NOAA, Boulder, CO, USA

14 ⁷I.M. Systems Group, Inc., Rockville, MD, USA

15 ⁸Environmental Modeling Center, NOAA/NWS/NCEP, College Park, MD, USA

16
17 *Correspondence to:* Cheng-Hsuan Lu (clu@ucar.edu; clu4@albany.edu)

18 **Abstract**

19 The Community Radiative Transfer Model (CRTM), a sensor-based radiative transfer model, has been used within the
20 Gridpoint Statistical Interpolation (GSI) system for directly assimilating radiances from infrared and microwave sensors. We
21 conducted numerical experiments to illustrate how including aerosol radiative effects in CRTM calculations changes the GSI
22 analysis. Compared to the default aerosol-blind calculations, the aerosol influences reduced simulated brightness temperature
23 (BT) in thermal window channels, particularly over dust-dominant regions. A case study is presented, which illustrates how
24 failing to correct for aerosol transmittance effects leads to errors in meteorological analyses that assimilate radiances from
25 satellite IR sensors. In particular, the case study shows that assimilating aerosol-affected BTs significantly affects analyzed
26 temperatures in the lower atmosphere across several regions of the globe. Consequently, a fully-cycled aerosol-aware
27 experiment improves 1-5 day forecasts of wind, temperature, and geopotential height in the tropical troposphere and Northern
28 Hemisphere stratosphere. Whilst both GSI and CRTM are well documented with online user guides, tutorials and code
29 repositories, this article is intended to provide a joined-up documentation for aerosol absorption and scattering calculations in
30 the CRTM and GSI. It also provides guidance for prospective users of the CRTM aerosol option and GSI aerosol-aware
31 radiance assimilation. Scientific aspects of aerosol-affected BT in atmospheric data assimilation are briefly discussed.

32 **1 Introduction**

33 An accurate and computationally efficient radiative transfer model is essential in radiance assimilation for supporting weather
34 prediction, physical retrievals for satellite environmental data records, and inter-comparison between different remote sensing
35 instruments. The Community Radiative Transfer Model (CRTM) is a radiative transfer model used extensively within satellite
36 and remote sensing systems (Weng, 2007; Han et al., 2007). It was primarily designed for computing satellite radiances and
37 has been widely used within the Gridpoint Statistical Interpolation (GSI, Wu et al., 2002; Kleist et al., 2009) system for directly
38 assimilating radiances from infrared (IR) and microwave (MW) sensors. Specifically, clear-sky radiance calculations are
39 carried out within the CRTM given the atmospheric scattering and absorption profile, surface emissivity and reflectivity, and
40 source functions. For cloudy radiance simulations (Stegmann et al., 2018), vertical profiles of hydrometeor variables (e.g.,
41 cloud liquid water path and ice water path) are also required. Note that the CRTM was not designed to enact composition-
42 radiation interaction effects within spectral longwave and shortwave radiative transfer calculations in general circulation
43 models. Instead, the CRTM was developed to support monochromatic satellite radiance assimilation from longwave and
44 microwave sensors, and for satellite retrieval algorithm development.

45
46 Past studies have demonstrated that aerosols significantly impact the simulation of brightness temperature (BT) in the IR
47 channels. BT is “a descriptive measure of radiation in terms of the temperature of a hypothetical blackbody emitting an
48 identical amount of radiation at the same wavelength” (American Meteorological Society, 2012). A reduction in retrieved BT
49 of 2-4 K in the atmospheric window region due to a strong dust outbreak was reported during the Saharan Dust Experiment
50 (SHADE) campaign (Highwood et al., 2003). Pierangelo et al. (2004) and Peyridieu et al. (2009) showed that the dust cooling
51 effects may reach 3 K in tropical atmospheric conditions depending on the dust burden. Diaz et al. (2001) found that there is
52 a significant increase in the errors of sea surface temperature (SST) retrievals in the presence of enhanced aerosol loading in
53 the atmosphere. The dust effects on satellite derived SST are constrained by accounting for dust absorption (Weaver et al.,
54 2003), applying a dust correction scheme (Nalli and Stowe, 2002; Merchant et al., 2006), or removing dust-contaminated
55 observations (Divakarla et al., 2012).

56
57 The impact of aerosol-affected BTs on the meteorological analysis fields has also been investigated. Wei et al. (2021a) used
58 the Global Data Assimilation System (GDAS, Kleist et al., 2009) to assess the aerosol impact on the meteorological analysis.
59 To do this, two GDAS experiments were conducted: a control cycled experiment, where aerosol transmittance effects are not
60 considered, and an offline non-cycled experiment, where aerosol transmittance effects are considered in the BT calculations.
61 The offline experiment uses identical observations and first guesses as the control experiment and thus the response of
62 atmospheric analysis to aerosol-aware radiance calculations can be clearly demonstrated. The experimental setup in Wei et al.
63 (2021a) followed the methodology presented in Kim et al. (2018), which is based on the Goddard Earth Observing System
64 (GEOS)-atmospheric data assimilation system (ADAS). Note that GEOS-ADAS and GDAS both used GSI and CRTM,

65 although the version and configuration differed. The studies by Kim et al. (2018) and Wei et al. (2021a) reported that: (i) a
66 considerable cooling effect on simulated BT when aerosols are considered; (ii) including aerosol transmittance effects in the
67 BT calculation improves the fit to observations over the dust-laden regions, and (iii) the offline aerosol-aware experiment
68 produces warmer analyzed SST (0.3 - 0.5 K) over the Atlantic Ocean. Wei et al. (2021a) also reported a warmer analysed
69 lower atmosphere (0.15 K) over Africa and the central Atlantic Ocean in the offline aerosol-aware experiment.

70

71 The experiments conducted in Kim et al. (2018) and Wei et al. (2021a) were based on the application of the CRTM aerosol
72 absorption and scattering routines. While aerosol absorption and scattering options are available from CRTM version 2.2
73 onwards; to our knowledge, the documentation of the CRTM aerosol module (Liu and Lu, 2016) has yet to be updated. Here
74 we presented a joined-up documentation for aerosol absorption and scattering calculations in the CRTM and GSI. In addition,
75 we provide guidance for prospective users of running aerosol-affected GSI analysis. Scientific aspects of aerosol-affected BT
76 in atmospheric data assimilation are also briefly discussed.

77 **2 GSI and CRTM**

78 Below, we provide a brief introduction to the GSI in section 2.1 and a description of the CRTM aerosol option in section 2.2.
79 In section 2.3, a description of running aerosol-aware GSI analysis is given.

80 **2.1 GSI**

81 The multi-partner-developed GSI is an incremental three-dimensional variational (3D-Var) data assimilation system (Wu et
82 al., 2002; Kleist et al. 2009). GSI, alone or combined with an ensemble system, has been used widely by modelling centers
83 and the research community for a range of research and applications. For instance, it is used operationally by the National
84 Oceanic and Atmospheric Administration (NOAA)/National Centers for Environmental Prediction (NCEP) for medium-range
85 weather forecast. It is also used by the National Aeronautics and Space Administration (NASA)/Global Modeling and
86 Assimilation Office (GMAO) for recent production of the Modern-Era Retrospective Analysis for Research and Applications,
87 version 2 (MERRA-2; Gelaro et al., 2017). The community version of the GSI system has been supported and maintained by
88 the Developmental Testbed Center (DTC; <http://www.dtcenter.org>). Note that DTC is scheduled to cease all activities
89 supporting the GSI user community by the end of December 2021. However, community GSI-related assets (website, forum,
90 and repository) built by DTC will remain available to and usable by the community.

91

92 GSI can assimilate a wide range of observations, including conventional observations (such as radiosonde observations), radar
93 data, satellite retrievals (for example global positioning system (GPS) radio occultation sounding data), satellite radiance data,
94 etc. For IR satellite instruments, GSI has the capability to assimilate radiances from Advanced Infrared Sounder (AIRS) on
95 AQUA, Infrared Atmospheric Sounding Interferometer (IASI) on METOP-A and METOP-B, Cross-track Infrared Sounder

96 (CrIS) on S-NPP, High resolution Infrared Radiation Sounder (HIRS) on METOP-A, METOP-B, and NOAA-19, Advanced
97 Very High Resolution Radiometer (AVHRR) on NOAA-18 and METOP-A, Spinning Enhanced Visible and Infrared Imager
98 (SEVIRI) on M08 and M10, and Geostationary Operational Environmental Satellite (GOES) Sounders (sndrD1, sndrD2,
99 sndrD3, and sndrD4) on GOES-15. A comprehensive list of all observations assimilated and monitored by GDAS can be found
100 at the webpage for “Observational Data Processing at NCEP” ([https://www.emc.ncep.noaa.gov/emc/pages/infrastructure/obs-](https://www.emc.ncep.noaa.gov/emc/pages/infrastructure/obs-data-processing.php)
101 [data-processing.php](https://www.emc.ncep.noaa.gov/emc/pages/infrastructure/obs-data-processing.php)).

102

103 Despite the broad applications of GSI, the publicly released version handles only clear-sky radiances for IR sensors. Without
104 correcting for aerosol transmittance effects, systematic biases may be introduced into the meteorological analysis fields when
105 observations affected by aerosols are assimilated. The aerosol-aware option (discussed in section 2.2) reduces such errors by
106 enabling aerosols to influence GSI's radiance observation operator, CRTM, which calculates the BT and Jacobians (radiance
107 1st derivative). This option, however, may fluctuate the amount of observations assimilated in GSI because the quality control
108 (QC) algorithm screens out observations based on measured BTs and aerosol-free simulated BTs. Thus, an improved QC
109 algorithm is needed to fully exploit radiance measurements under all sky conditions. The technical issues regarding the QC
110 procedure have been discussed in Kim et al. (2018) and Wei et al. (2021 a).

111 **2.2 CRTM aerosol module**

112 The CRTM, a one-dimensional radiative transfer model (Liu and Weng, 2006), is developed at the U.S. Joint Center for
113 Satellite Data Assimilation (JCSDA) with algorithm and software input from JCSDA collaborating research institutions. The
114 CRTM is composed of four modules, which include gaseous transmittance, surface emission and reflection, cloud and aerosol
115 absorption and scattering, and a solver for radiative transfer (Han et al., 2006). Given an atmospheric profile of temperature,
116 cloud and surface properties, and gaseous constituents and aerosol concentrations, the CRTM is called within the GSI to
117 calculate BTs for satellite sensors from IR sounders to MW imagers. Here, we describe the aerosol scattering and absorption
118 scheme in CRTM version 2. We refer the readers to Han et al. (2006) for the full details regarding CRTM version 1.

119

120 Absorption by atmospheric trace gases, such as water vapor and carbon dioxide, is parameterized using the Optical Depth in
121 Absorber Space (ODAS) and the Optical Depth in Pressure Space (ODPS) algorithms (Chen et al., 2012), which are based on
122 rigorous line-by-line calculations from the Line-By-Line Radiative Transfer Model (LBLRTM, Clough et al., 1992). For
123 enacting aerosol attenuation effects, the CRTM uses pre-computed lookup tables, which calculate aerosol optical properties,
124 specifically the extinction coefficient, single-scattering albedo, asymmetry factor, and phase function coefficients. The CRTM
125 version 2.2 and 2.3 contain the optical look-up table based on the aerosol types of the mass-based Goddard Chemistry Aerosol
126 Radiation and Transport (GOCART, Chin et al., 2002; Colarco et al, 2010) module, for their radiative effects from the
127 ultraviolet to the infra-red. Operationally, given aerosol types, radius, concentration and ambient relative humidity, CRTM
128 generates aerosol optical profiles that the radiative transfer solver requires for multi-scattering simulations and radiance

129 calculations. The effect of aerosols on MW sensors is not considered yet because the impact of aerosols on MW radiance is
 130 usually very small, given aerosols size is generally much smaller than MW wavelengths (Petty, 2006). There are ongoing and
 131 planned CRTM development efforts to incorporate more aerosol optical tables (such as the Community Multiscale Air Quality
 132 model, CMAQ). With the expansion of the aerosol schemes, a new releasing and versioning system for optical tables is
 133 essential and currently under discussion. This article, however, discusses mainly the GOCART model, which is the default
 134 aerosol scheme in the CRTM version 2.

135

136 The GOCART model (Chin et al., 2002; 2014), a bulk aerosol scheme, simulates major tropospheric aerosol components,
 137 including dust, sea salt, black carbon (BC), organic carbon (OC) and sulfate. It is one of the most widely used aerosol modules
 138 in the Weather Research and Forecasting model coupled with Chemistry (WRF-Chem; see Ukhov et al. (2021) and references
 139 therein). It is used in the GEOS framework at GMAO for near-real-time aerosol forecasts (Colarco et al., 2010) as well as in
 140 MERRA reanalysis (Buchard et al., 2015) and MERRA-2 reanalysis (Randles et al., 2017). It is also implemented in the Global
 141 Forecast System (GFS) framework at NCEP (Lu et al., 2016; Wang et al., 2018; Zhang et al., 2021) for near-real-time global
 142 aerosol forecasts.

143

144 When GOCART was selected as the aerosol module within WRF-Chem, it was configured with fourteen GOCART aerosol
 145 species (Liu et al., 2011): sulfate; hydrophobic and hydrophilic OC and BC; sea salt in four particle size bins (with radii of
 146 0.1-0.5, 0.5-1.5, 1.5-5, and 5-10 μm) and dust particles in five particle size bins (with radii of 0.1-1.0, 1.0-1.8, 1.8-3, 3-6, and
 147 6-10 μm). A default CRTM lookup-table has been used for pre-calculated aerosol optical property parameters for the fourteen
 148 GOCART aerosol species (Liu et al., 2007; Liu and Lu, 2016). We assume that the particles are spherical and externally mixed.
 149 We also assume lognormal size distributions for sulfate and carbonaceous aerosols as well as for each sea salt and dust bin.
 150 The lognormal size distribution for N particles can be expressed as follows (d'Almeida et al., 1991),

$$151 \quad n(\ln r) = \frac{N}{\sqrt{2\pi \ln(\sigma_g)}} \exp\left[-\frac{1}{2} \left(\frac{\ln r - \ln r_g}{\ln(\sigma_g)}\right)^2\right], \quad (1)$$

152 where r is a radius, r_g the geometric median radius, and σ_g the geometric mean standard deviation. The k^{th} moment of the
 153 distribution can be expressed as follows (Binkowski and Roselle, 2003),

$$154 \quad M_k = \int_{-\infty}^{\infty} r^k n(\ln r) d\ln(r) = r_g^k \exp\left[\frac{k^2}{2} \ln^2(\sigma_g)\right]. \quad (2)$$

155 where M_0 is the number N of aerosol particles, and M_2 and M_3 are proportional to the total particulate surface area and volume,
 156 respectively. Thus, the effective radius (r_{eff}) can be defined as

$$157 \quad r_{\text{eff}} = \frac{M_3}{M_2} = r_g \exp\left[\frac{5}{2} \ln^2(\sigma_g)\right]. \quad (3)$$

158

159 Table 1 lists the GOCART size parameters (particle density, effective radius, and geometric standard deviation) and refractive
 160 indices at 550 nm used in CRTM version 2. The optical properties of each aerosol species are computed based on Mie scattering
 161 theory. Hydrophilic aerosol particle size increases as relative humidity (RH) of the ambient atmosphere increases. Therefore,
 162 the water content in aerosol needs to be considered when calculating the refractive index. The effective radius growth factor
 163 for hygroscopic aerosols may be theoretically calculated or obtained from a pre-calculated look-up table (d’Almeida et al.,
 164 1991). In this study, the hygroscopic growth factor used for the GOCART model (Chin et al., 2002) is adopted and given in
 165 Table 2. Once the growth factor a_g is evaluated, the refractive index n_r for the hygroscopic aerosol can be calculated using a
 166 volume mixing method as:

$$n_r = n_w + (n_o - n_w) \times a_g^3 \quad (4)$$

168 where n_o and n_w are the refractive indices for dry aerosols and water, respectively. We adopt the refractive index n_o from the
 169 Optical Properties of Aerosols and Clouds (OPAC) dataset (Hess et al. 1998), while the water refractive index is given by
 170 (Hale and Querry, 1973).

171
 172 **Table 1.** Goddard Chemistry Aerosol Radiation and Transport (GOCART) size distribution parameters and refractive indices
 173 at 550 nm for dry aerosols.

Aerosol type	Density [g cm ⁻³]	Effective radius r_{eff} [μm]	Standard deviation σ [μm]	Refractive index real part $n(\lambda)$	Refractive index imaginary part $k(\lambda)$
Sulfate	1.7	0.242	2.03	1.43	1.00×10^{-8}
OC1 (hydrophobic)	1.8	0.087	2.20	1.53	6.00×10^{-3}
OC2 (hydrophilic)	1.8	0.087	2.20	1.53	6.00×10^{-3}
BC1 (hydrophobic)	1.0	0.036	2.0	1.75	4.40×10^{-1}
BC2 (hydrophilic)	1.0	0.036	2.0	1.75	4.40×10^{-1}
SeaSalt1 (size range)	2.2	0.3	2.03	1.50	1.00×10^{-8}
SeaSalt2	2.2	1.0	2.03	1.50	1.00×10^{-8}
SeaSalt3	2.2	3.25	2.03	1.50	1.00×10^{-8}
SeaSalt4	2.2	7.5	2.03	1.50	1.00×10^{-8}
Dust1 (size range)	2.6	0.65	2.0	1.53	5.50×10^{-3}
Dust2	2.6	1.4	2.0	1.53	5.50×10^{-3}
Dust3	2.6	2.4	2.0	1.53	5.50×10^{-3}
Dust4	2.6	4.5	2.0	1.53	5.50×10^{-3}
Dust5	2.6	8.0	2.0	1.53	5.50×10^{-3}

174
 175 **Table 2.** Hygroscopic aerosol growth factor a_g as a function of the ambient relative humidity (RH).

RH(%)	0	50	70	80	90	95	99

Sulfate	1.0	1.4	1.5	1.6	1.8	1.9	2.2
Organic Carbon	1.0	1.2	1.4	1.5	1.6	1.8	2.2
Black Carbon	1.0	1.0	1.0	1.2	1.4	1.5	1.9
Sea Salt	1.0	1.6	1.8	2.0	2.4	2.9	4.8

176

177 The GOCART model used by GMAO and NCEP for aerosol forecast and reanalysis has evolved to use 5 sea salt size bins
 178 (with radii of 0.03-0.1, 0.1-0.5, 0.5-1.5, 1.5-5, and 5-10 μm). The first sub-micron sea salt bin was added to facilitate optical
 179 properties and aerosol-cloud interaction studies (Colarco et al., 2010), but was excluded from the previous GOCART versions
 180 as well as the WRF-Chem GOCART model. While GMAO’s GEOS and NCEP’s GFS contain fifteen GOCART aerosol
 181 species, the CRTM aerosol module has also not yet been modified to include the new added sub-micron sea salt bin (see Table
 182 1). To overcome this discrepancy, the latest GSI/CRTM release (i.e., GSI 3.7 and CRTM 2.3) combines the mixing ratios from
 183 the two sub-micron sea salt bins in order to use the aerosol optical property parameters from the original GOCART model.
 184 This limitation is acknowledged in this article and will be addressed in a future CRTM release (see section 4).

185

186 While the CRTM is primarily designed for computing satellite radiances, an additional module was added to CRTM by Liu
 187 and Lu (2016) to compute aerosol optical depth (AOD). This CRTM-AOD module enables the GSI system to assimilate AOD
 188 observations (Liu et al., 2011; Schwartz et al., 2012; Pagowski et al., 2014). This article, however, is focused on the observation
 189 operator for radiance, and we refer the reader to Pagowski et al. (2014) for the description of the AOD observation operator
 190 and GSI AOD data assimilation.

191 **2.3 Running aerosol-aware GSI analysis**

192 The operational version of GSI maintained by NOAA/NCEP Environmental Modeling Center (EMC) is utilized in the present
 193 study. Its source code and associated static files are distributed through the GitHub repository (<https://github.com/NOAA-EMC/GSI>). An open-access archive of source code and data is described in Code and Data Availability. To run the GSI
 194 analysis, the reader can refer to the user guide for GSI v3.7 (the latest released version as of April 2021), which is available at
 195 https://dtcenter.ucar.edu/com-GSI/users/docs/users_guide/html_v3.7/index.html. In addition, an online tutorial is available at
 196 https://dtcenter.ucar.edu/com-GSI/users/tutorial/online_tutorial/index_v3.7.php. For CRTM, the user guide and tutorials can
 197 be found at <https://www.jcsda.org/jcsda-project-community-radiative-transfer-model>. Thus, only a brief description of
 198 aerosol-affected BT calculations is given.

200

201 A regression test “global_C96_fv3aerorad” has been introduced into NOAA/EMC GSI code repository (pull request #32) to
 202 assure the functionality of aerosol-aware BT derivations in GSI/CRTM works as expected. This regression test uses a sample
 203 background file taken from the aerosol member of the Global Ensemble Forecast System (GEFS-Aerosol; Zhang et al., 2021).
 204 All fifteen GOCART aerosol species are passed along to the CRTM. In addition to the background file, a user needs to modify

205 the configuration files, anavinfo and satinfo, in the “fix” directory. The anavinfo file is the information file to set control and
206 analysis variables. The satinfo file is the information file to specify satellite channels to be assimilated and associated
207 parameters. For an aerosol-aware experiment where aerosol absorption and scattering are included in BT calculations, aerosol
208 species are specified in the “chem_guess” section of anavinfo and sensors and channels are set to 1 in the “iaerosol” column
209 of satinfo. The reader can refer to the fv3aerorad_satinfo.txt and anavinfo_fv3aerorad for the aerosol-aware configuration. The
210 corresponding namelist (gsiparm.anl) can be found at the “global_C96_fv3aerorad” section (line 2931–3046) in
211 regression_namelist.sh under the “regression” directory. It should be noted that the namelist variable, “lread_ext_aerosol”,
212 determines how GSI ingests the aerosol information from background files or external files.

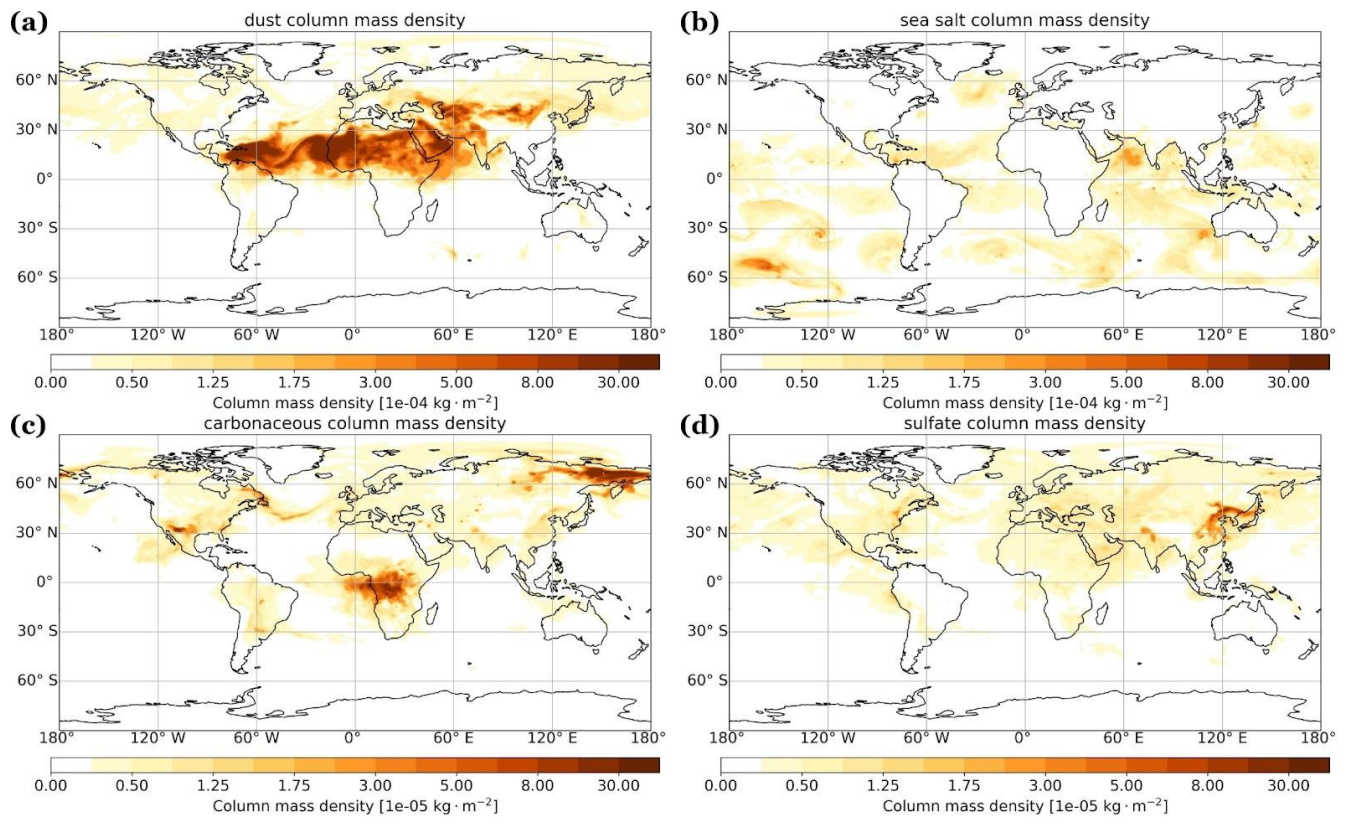
213 **3. Numerical Results**

214 **3.1 Aerosol impacts on BT calculations**

215 To illustrate how an aerosol transmittance correction is required within satellite radiances assimilated into meteorological data
216 assimilation systems, we present a detailed analysis of a single-cycle GSI experiment (the AER experiment) using GOCART
217 fields from MERRA-2 on 12Z June 22, 2020. This time is chosen because it captures a strong Saharan dust event that covers
218 the trans-Atlantic region. A baseline GSI experiment (the CTL experiment) with the anavinfo and satinfo resource files reverted
219 back to the default aerosol-blind configuration was also conducted. Both experiments used the same first-guess fields and
220 assimilated identical conventional and satellite observations within a ± 3 -hour assimilation window. In AER, the aerosol
221 transmittance effects were only considered in the CRTM simulation for IR sensors.

222
223 Figure 1 shows the global aerosol column mass density distribution from MERRA-2 during 12Z June 22, 2020. The panels a,
224 b, c, and d depict dust, sea salt, carbonaceous and sulfate, respectively. Dust plumes spread over northern Africa, the tropical
225 Atlantic Ocean, the Middle East, and northwestern China. Wind-driven sea salt aerosols are seen over tropical and southern
226 hemisphere oceans. Carbonaceous and sulfate aerosols mainly appear in areas with extensive biomass burning and fuel
227 combustion activities (note one order smaller than dust and sea salt). The overall aerosol loading is dominated by mineral dust.
228 Wu et al. (2020) evaluated the dust spatiotemporal variations of MERRA-2 against satellite observations and global model
229 simulations. They found that MERRA-2 agrees well with satellite observations due to the assimilation of satellite AOD. But
230 in North America and the Arctic, the dust burden in MERRA-2 is much larger than those in other models despite having similar
231 dust emissions fluxes. The high dust burden over these regions is due to higher mass fraction of fine dust and enhanced dust
232 transport. Furthermore, Bullard et al. (2016) reported that large gaps exist in our understanding of basic characteristics of high-
233 latitude dust sources. This highlights the importance of representing aerosol emissions, transport, removal, and size distribution
234 in global models in correctly simulating aerosol spatiotemporal distributions.

235



236

237 **Figure 1.** Aerosol column mass density (kg m^{-2}) from MERRA-2 on 12Z June 22, 2020: (a) dust, (b) sea salt, (c) carbonaceous,
 238 and (d) sulfate.

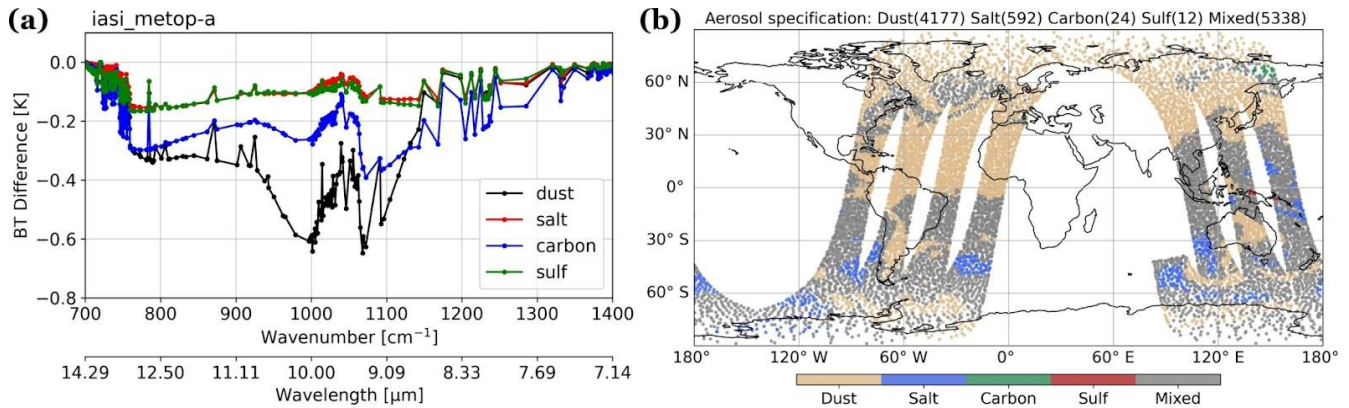
239

240 Figure 2a shows the first-guess BT differences of IASI onboard METOP-A between the two experiments (AER – CTL) in the
 241 IR atmospheric window channels over dust, sea salt, carbonaceous and sulfate dominant regions. The stratification criterion
 242 for each type is where the fraction of column mass density of dominant species, from MERRA-2, is larger than 0.65 (shown
 243 in Fig. 2b). Figure 2a shows that dust aerosols generate the stronger cooling effects, about 0.7 K at the thermal IR window
 244 region ($\sim 10 \mu\text{m}$), than other species. The importance of correcting for aerosol transmittance effects within BT algorithms has
 245 been reported in previous studies (Sokolik, 2002; Weaver et al., 2003; Pierangelo et al., 2004; Matricardi, 2005; Merchant et
 246 al., 2006; Kim et al., 2018; Wei et al., 2021a). Table 3 describes the range and the average of total aerosol column mass density
 247 over the regions with different dominant aerosol species. It shows that the total loading of aerosols is similar over the dust and
 248 carbonaceous aerosols dominated regions. This indicates that the stronger cooling effects by dust aerosol on BT in the IR
 249 window region is not due to stronger loading. Note that in the northern hemisphere, the high-latitude region is characterized
 250 as dust-dominant except for the Russian Far East in MERRA-2 (Figure 2b). While anomalous or erroneous modeled aerosol
 251 loading may bias the results, the finding that dust has the largest impact on the BTs simulations, reported in this study and

252 previous studies, remains unchanged. Therefore, we focus our remaining analysis on dust over Tropical Africa and the Mid-
 253 Atlantic.

254

255



256

257 **Figure 2.** (a) The differences (AER-CTL) of first-guess brightness temperatures in the IR window region of IASI onboard
 258 METOP-A. (b) The corresponding regions dominated by different aerosol species from the 12Z June 22, 2020. The data counts
 259 for each species are labelled in panel (b).

260

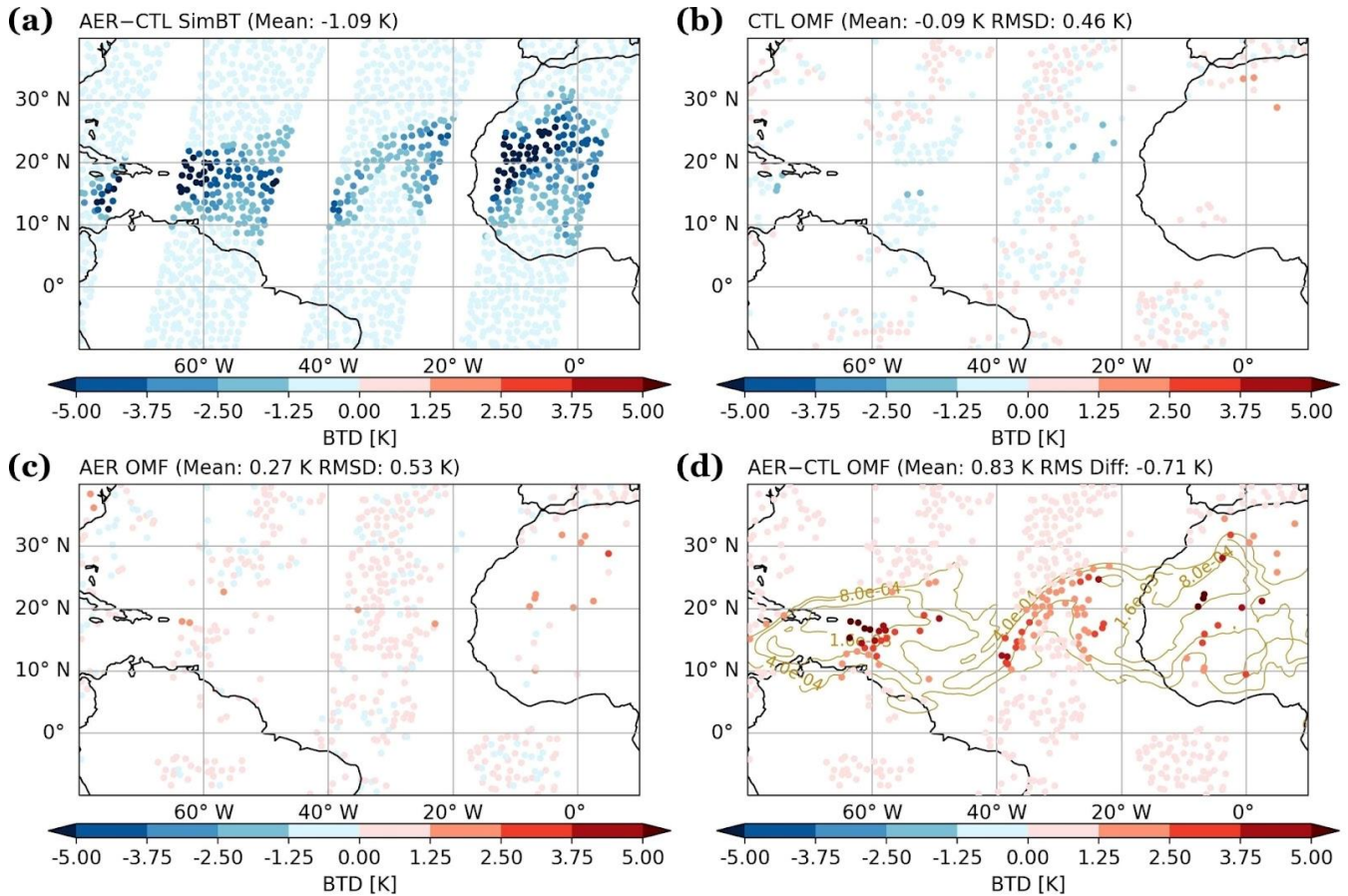
261 **Table 3.** The range of aerosol column mass density (kg/m^2) from MERRA-2 at the regions dominated by different aerosol
 262 species (fraction over 0.65) of IASI onboard METOP-A at the cycle of 12Z June 22, 2020.

Dominant aerosol species	Column mass density (kg/m^2)				
	Minimum	Maximum	Mean	Median	SD
Dust	2.69e-06	2.88e-03	1.76e-04	4.20e-05	3.59e-04
Sea salt	4.91e-06	4.01e-05	1.68e-05	1.59e-05	6.15e-06
BC+OC	1.04e-05	6.07e-04	1.76e-04	1.52e-04	1.20e-04
Sulfate	6.45e-06	9.53e-05	2.15e-05	1.28e-05	2.46e-05

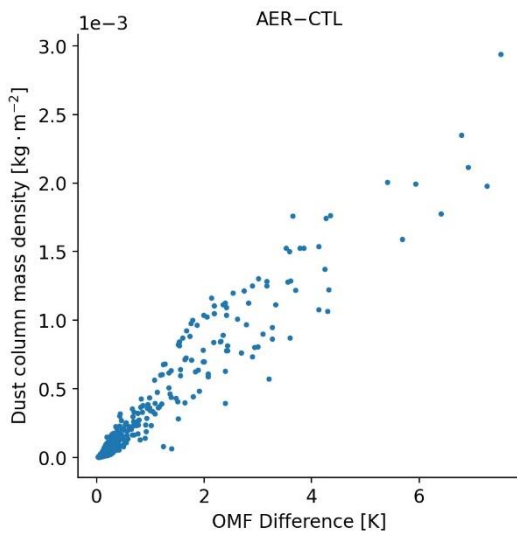
263

264 Figure 3 displays the AER - CTL difference in the simulated BTs and their respective first-guess departures (observed minus
 265 first guess, OMF) calculated at the 10.39 μm channel from IASI onboard METOP-A. The Figure focuses on North Africa and
 266 the trans-Atlantic region, where a large dust plume spans the region. Significant aerosol cooling (~ 4 K) in BT was found in
 267 the aerosol-aware experiment (Fig. 3a) due to the large plume. Comparing the first guess departures from CTL and AER
 268 experiments (Fig. 3b and 3c) shows that OMFs for AER are warmer than CTL (cf. 0.27 K vs. -0.09 K). Note that some
 269 observations assimilated in CTL were rejected in AER (near 55° W and 15° N) and vice versa (near 65° W and 15° N, and

270 over Africa). This feature suggests that the quality control has been influenced by including aerosol transmittance effects in
 271 CRTM. Over the trans-Atlantic region, the aerosol-aware experiment assimilated several observations with larger first-guess
 272 departures located in the strong dust plume (Fig. 3d). Figure 4 presents the scatter plot of dust column mass density versus
 273 OMF differences (AER - CTL) for these data points assimilated in AER on 12Z June 22, 2020. The data points with large
 274 OMF differences are corresponding to the areas with higher dust loading. Nevertheless, when considering aerosol information,
 275 the root-mean-square first-guess departures decreased 0.08 K globally and 0.42 K over the trans-Atlantic region at this channel
 276 (not shown here). This implies that simulated BTs in the aerosol aware run are in better agreement with the observations.
 277
 278



279
 280 **Figure 3.** (a) Simulated BT differences (AER - CTL), (b) bias-corrected OMF from the CTL experiment, (c) bias-corrected
 281 OMF from the AER experiment, and (d) OMF differences (AER - CTL) for 10.39 μm channel of IASI onboard METOP-A.
 282 All the data are from the analysis cycle on 12Z June 22, 2020. Contours of total column mass density from MERRA-2 are
 283 plotted in panel (d).



284

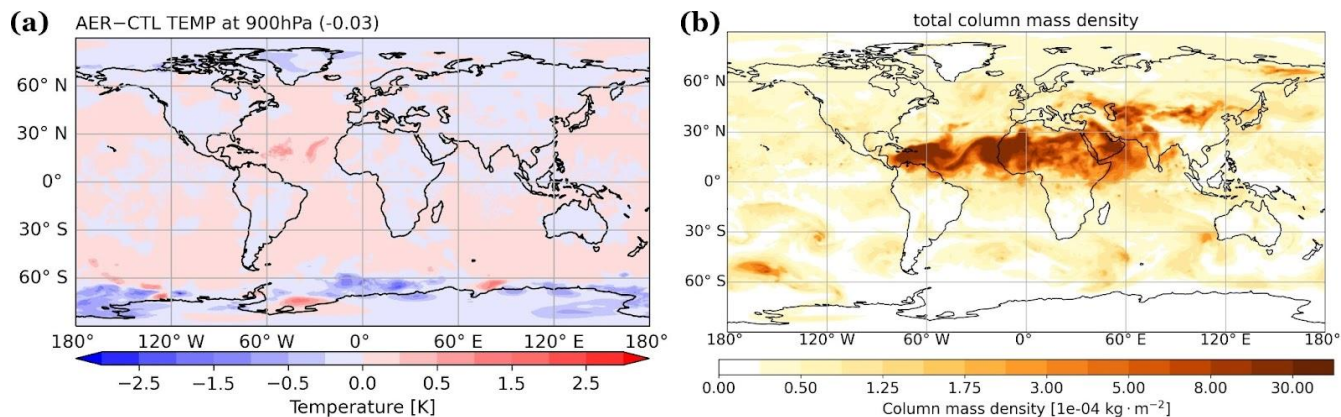
285 **Figure 4.** The scatter plot of dust column mass density from MERRA-2 against the first-guess departure differences (AER –
 286 CTL) assimilated in AER experiment (without bias correction) on 12Z June 22, 2020.

287

288 Figure 5 shows (a) the global differences in analyzed temperature at 900 hPa between the two experiments and (b) the total
 289 aerosol column mass density incorporated in the GSI/CRTM system. When aerosol transmittance effects are considered in the
 290 BT calculations, the air temperatures are not only adjusted over aerosol-laden regions but also across the globe. The impact is
 291 shown outside aerosol-active regions, which could be attributed to the change from the spatial correlation in the GSI
 292 background error covariance. Over the trans-Atlantic region where the dust loading is high (shown in Figure 1a), the AER
 293 experiment produces 0.5 K to 1 K of warming relative to CTL. As dust travels off the west coast of Africa into the Atlantic,
 294 the particles are lifted and carried by the Saharan Air Layer (SAL), around 800 – 600 hPa (Diaz et al., 1976; Karyampudi et
 295 al., 1999). In the case of 12Z June 22, 2020, MERRA-2 captured the dust transport within SAL, and air mass is increasingly
 296 composed of fine dust particles due to the gravitational settling of coarser particles (not shown here). Wei et al. (2021b)
 297 conducted a series of CRTM v2.3 experiments using idealized dust profiles and reported that mass loading and the altitude of
 298 the dust layer are the primary and secondary factors affecting the BT simulations, respectively; changes in the fine versus
 299 coarse particle partition show little influence on the BT simulations. Based on these results we speculate that elevated dust
 300 plume retains unneglected influences on BT calculations (Figure 3a). Experiments with robust estimated aerosol distributions
 301 over extended time period are needed to quantify the sensitivity of GSI analysis to aerosol-aware CRTM calculations. This
 302 manuscript, however, is intended to provide a joined-up documentation for the CRTM aerosol option and thus unravelling
 303 these questions is beyond the scope of this study.

304

305



306

307 **Figure 5.** (a) The differences (AER - CTL) of analyzed temperature (K) at 900 hPa and (b) the corresponding aerosol column
 308 mass density ($\text{kg} \cdot \text{m}^{-2}$) from MERRA-2 on 12Z June 22, 2020.

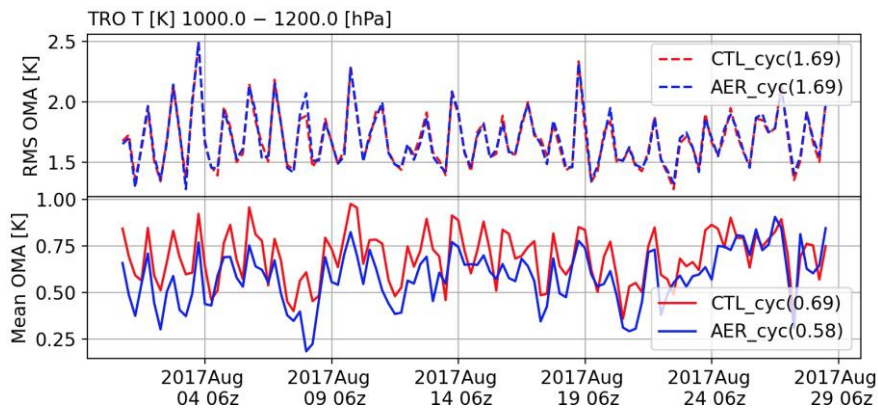
309 3.2 Aerosol impacts on the analysis

310 The experiments reported in this section were produced with the NCEP GFS version 14 and the corresponding GDAS. Our
 311 experiments used a coarser resolution, T670 ($\sim 30 \text{ km}$) for the model and T254 ($\sim 80 \text{ km}$) for the analysis, different from the
 312 NCEP operational GFSv14 configuration at T1534 ($\sim 13 \text{ km}$) and T574 ($\sim 27 \text{ km}$). The experiments covered the August 2017
 313 period, initialized from NCEP's archived GDAS analysis on July 25 00Z. The analysis cycles every 6 hours (at 00z, 06z, 12z,
 314 and 18z), with a ± 3 -hour assimilation window and continuous data utilization. The control experiment (CTL_cyc) was an
 315 aerosol-blind fully cycled experiment where aerosol effects on radiances are not considered (as is by default). The aerosol
 316 experiment (AER_cyc) was an aerosol-aware fully cycled experiment where aerosol-affected satellite radiances are taken into
 317 account. Here, we used CRTM version 2.2.4. Time-varying 3-dimensional GOCART aerosols were taken from NCEP's
 318 archived NEMS GFS Aerosol Component (NGAC) v2 (Wang et al., 2018).

319

320 Figure 6 displays the statistics of analysis departures (observation minus analysis, OMA) from CTL_cyc and AER_cyc to
 321 evaluate the performance of temperature analysis at the lower atmosphere over the tropical region ($20^\circ \text{S} - 20^\circ \text{N}$). The positive
 322 value of mean OMAs indicates that both experiments have cold biases in the tropical region. It shows neutral impact on root-
 323 mean-square (RMS) and slightly positive impact on the cold biases. The latter implies that the departure of temperature analysis
 324 becomes larger when considering aerosol transmittance effects during the data assimilation (i.e., AER_cyc).

325



326

327 **Figure 6.** The comparison of the RMS and mean analysis departures (observation minus analysis, OMA) against in-situ
 328 measurements (e.g., radiosonde) of temperature with pressure over 1,000 hPa at the tropical region (20° S – 20° N) during 00Z
 329 August 1 – 18Z August 28, 2017.

330

331 Medium-range forecasts of AER_cyc are examined against CTL_cyc using the verification package from NOAA/NCEP EMC
 332 (https://www.emc.ncep.noaa.gov/gmb/STATS_vsdb). Figure 7 displays the scorecard of anomaly correlation and root-mean-
 333 square error (RMSE) for the day-1, -3, and -5 forecasts over August 1 – 28, 2017. Anomaly correlation coefficients show
 334 neutral to positive impact on day-1 forecasts of wind and temperature fields when aerosol cooling effects in BTs are considered.
 335 The RMSE scorecards show the forecast improvements in the wind, temperature and height fields throughout the troposphere
 336 over the Tropics (20° S – 20° N) and at upper level over the Northern Hemisphere (20° N – 80° N). For the Southern hemisphere
 337 (20° S – 80° S), however, there is neutral impact or degradation in the forecasts, which is likely due to cloud contamination
 338 and mixture of sea salt and aged smoke/sulfate aerosols. Compared to both hemispheres, the tropical forecasts show the most
 339 improved statistics in the aerosol-aware analysis, which may be attributed to larger aerosol loading in this region. While the
 340 RMSE scorecard focuses on background (i.e., time-averaged) fields, it should be noted that evaluation of the aerosol impacts
 341 on the analysis and forecasts of African easterly wave that developed Hurricane Harvey and Gert in 2017 is presented in
 342 Grogan et al. (2021).

343

		Globe			N. Hemisphere			S. Hemisphere			Tropics				
		Day 1	Day 3	Day 5	Day 1	Day 3	Day 5	Day 1	Day 3	Day 5	Day 1	Day 3	Day 5		
Anomaly Correlation	Heights	250hPa													
		500hPa													
		700hPa													
		1000hPa													
	Vector Wind	250hPa	▲												
		500hPa	▲												
		850hPa	▲												
	Temp	250hPa	▲												
		500hPa		▼							▼				
		850hPa	▲												
RMSE	Heights	10hPa	▲	▲	▲		▲	▲				▲	▲	▲	
		20hPa	▲	▲	▲	▲	▲	▲				▲	▲	▲	
		50hPa	▲	▲	▲	▲	▲	▲	▲				▲	▲	▲
		100hPa	▲	▲	▲	▲	▲					▲	▲	▲	
		200hPa	▲										▲	▲	▲
		500hPa											▲	▲	▲
		700hPa													
		850hPa													
		1000hPa													
		Vector Wind	10hPa	▲	▲		▲	▲	▲					▲	▲
	20hPa		▲	▲		▲	▲	▲	▲	▲	▲		▲	▲	▲
	50hPa		▲	▲	▲	▲	▲	▲	▲	▲			▲	▲	▲
	100hPa		▲	▲	▲	▲	▲	▲	▲	▲	▲		▲	▲	▲
	200hPa		▲			▲							▲	▲	
	500hPa		▲										▲	▲	
	700hPa		▲										▲	▲	
	850hPa		▲										▲	▲	
	1000hPa		▲										▲	▲	
	Temp		10hPa	▲	▲		▲	▲						▲	▲
		20hPa	▲	▲		▲	▲	▲	▲	▲			▲	▲	▲
		50hPa	▲	▲		▲	▲	▲	▲	▲	▲		▲	▲	▲
		100hPa	▲	▲	▲	▲	▲						▲	▲	▲
		200hPa	▲			▲							▲	▲	▲
		500hPa													
		700hPa													
		850hPa	▲			▲							▲	▲	
		1000hPa	▲			▲							▲	▲	

344

345

346

347

348

349

Figure 7. Scorecard of anomaly correlation and RMSE of comparison between AER_cyc and CTL_cyc. Green colors mean AER_cyc is better than CTL_cyc at 95% (filled box), 99% (▲), and 99.9% (▲) significance level. Red colors mean AER_cyc is worse than CTL_cyc at 95% (filled box), 99% (▼), and 99.9% (▼) significance level. Grey boxes mean no statistically significant difference between AER_cyc and CTL_cyc. Blue boxes are not statistically relevant. The statistics are calculated between 20 to 80 degrees of latitude for both hemispheres. The data between 20°S and 20°N is used for the tropical region.

350

4. Conclusions and Future Outlook

351

352

353

This article described aerosol absorption and scattering calculations of the CRTM version 2 in the GSI analysis. We also conducted sensitivity experiments to investigate the aerosol-affected GSI analysis in both single-cycle and fully-cycled runs. Both GSI and CRTM are well documented with user guides, tutorials and code repositories available online. This article is

354 primarily a joined-up documentation for aerosol absorption and scattering calculations in the CRTM version 2 and GSI. It also
355 provides guidance for prospective users of the CRTM aerosol option. Scientific aspects of aerosol-affected BT in atmospheric
356 data assimilation are briefly discussed. Specifically, numerical experiments were conducted to illustrate how including aerosol
357 radiative effects in CRTM changes the GSI analysis. We found that taking the aerosols into account reduces simulated BT in
358 thermal window channels over dust-dominant regions. Assimilating aerosol-affected BTs produces a warmer analyzed lower
359 atmosphere. From the verification scorecard, neutral to positive results are found in the fully-cycled, aerosol aware experiment.

360

361 The CRTM team, in coordination with its partners and collaborators, is building a robust capability to accurately and
362 consistently simulate the emission, absorption, and scattering properties of all (radiatively important) atmospheric constituents.
363 There are several ongoing and planned efforts to enhance the CRTM aerosol module. For example, more aerosol optical look-
364 up tables have been added and the calculations of aerosol optical properties are being evaluated. In addition, the CRTM is
365 being refactored toward a more flexible aerosol interface to handle aerosol optical look-up-tables as well as to support aerosol
366 specifications from other operational aerosol models, such as Community Multiscale Air Quality (CMAQ). Other aerosol-
367 related efforts include, but are not limited to, improving the physical representation of aerosols and including active sensors
368 such as aerosol lidar. These developments, once implemented and tested, will be reported in future manuscripts.

369 **Code and Data Availability.**

370 Various software packages are referred to throughout the paper. The following list contain links to the main software
371 documentations or repositories discussed:

372 The GSI webpage: <https://dtcenter.ucar.edu/com-GSI/users/index.php>

373 The GSI v3.7 user guide: https://dtcenter.ucar.edu/com-GSI/users/docs/users_guide/html_v3.7/index.html

374 The GSI v3.7 online tutorial: https://dtcenter.ucar.edu/com-GSI/users/tutorial/online_tutorial/index_v3.7.php

375 The DTC community GSI (as of Nov. 29, 2021, via Zenodo): <https://doi.org/10.5281/zenodo.5735601>

376 The CRTM v2.3.0 public repository (via Zenodo): <https://doi.org/10.5281/zenodo.5695707>

377 The aerosol related Fortran code in GSI:

378 Aerosol files check (when `lread_ext_aerosol` is true): `./src/gsi/read_files.f90`

379 Aerosol data ingestion: `./src/gsi/ncepnmns_io.f90`, `./src/gsi/general_read_nemsaero.f90`

380 CRTM simulation: `./src/gsi/crtm_interface.f90`

381 Effective radius setup: `./src/gsi/set_crtm_aerosolmod.f90`

382 **Author Contributions.**

383 QL implemented the aerosol module, CL designed the experiments, and SW performed the experiments. CL prepared the
384 manuscript with contributions from all co-authors.

385 **Acknowledgements.**

386 The study of CTL and AER cycled experiments are supported by the Next Generation Global Prediction System (NGGPS)
387 program within NOAA/NWS (award number 352 NA15NWS4680008). The testing and refinement of GSI/CRTM regression
388 test is supported by the DTC Visitor Program. All experiments were conducted at NOAA/NESDIS-funded Supercomputer for
389 Satellite Simulations and Data Assimilation Studies (S4) cluster maintained by Space Science and Engineering Center (SSEC)
390 at University of Wisconsin-Madison. We thank GMAO collaborators, Arlindo da Silva, Mian Chin, and Peter Colarco, for
391 providing valuable input on the calculations of aerosol optical properties for GOCART aerosols.

392 **References**

- 393 d'Almeida, G. A., Koepke, P., and Shettle, E.P.: Atmospheric Aerosols: global climatology and radiative characteristics, A.
394 Deepak Publishing, Hampton, VA., 1991.
- 395 American Meteorological Society: Brightness Temperature. Glossary of Meteorology,
396 https://glossary.ametsoc.org/wiki/Brightness_temperature, 2012.
- 397 Binkowski, F. S., Roselle, S. J.: Models-3 Community multiscale air quality (CMAQ) model aerosol component, 1 Model
398 description. *J. Geophys. Res.*, 108, 4183, doi:10.1029/2001JD001409, 2003.
- 399 Buchard, V., da Silva, A. M., Colarco, P. R., Darmonov, A., Randles, C. A., Govindaraju, R., Torres, O., Campbell, J., and
400 Spurr, R.: Using the OMI aerosol index and absorption aerosol optical depth to evaluate the NASA MERRA Aerosol
401 Reanalysis. *Atmos. Chem. Phys.*, 15, 5743–5760, doi:10.5194/acp-15-5743-2015, 2015.
- 402 Bullard, J. E. and Coauthors: High-latitude dust in the Earth system, *Rev. Geophys.*, 54, 447–485, doi:10.1002/
403 2016RG000518, 2016.
- 404 Chen, Y., Weng, F., Han, Y., and Liu, Q.: Planck-Weighted Transmittance and Correction of Solar Reflection for Broadband
405 Infrared Satellite Channels. *J. Atmos. Sci.* 29, 382-396, 2012.
- 406 Chin, M., Ginoux, P., Kinne, S., Torres, O., Holben, B. N., Duncan, B. N., Martin, R. V., Logan, J. A., and Higurashi, A.:
407 Tropospheric aerosol optical thickness from the GOCART model and comparisons with satellite and Sun photometer
408 measurements, *J. Atmos. Sci.*, 59, 461–483, doi:10.1175/1520-0469(2002)059<0461:TAOTFT>2.0.CO;2, 2002.
- 409 Chin, M., Diehl, T., Tan, Q., Prospero, J. M., Kahn, R. A., Remer, L. A., Yu, H., Sayer, A. M., Bian, H., Geogdzhayev, I. V.,
410 Holben, B. N., Howell, S. G., Huebert, B. J., Hsu, N. C., Kim, D., Kucsera, T. L., Levy, R. C., Mishchenko, M. I., Pan, X.,
411 Quinn, P. K., Schuster, G. L., Streets, D. G., Strode, S. A., Torres, O., and Zhao, X.-P.: Multi-decadal aerosol variations

412 from 1980 to 2009: a perspective from observations and a global model, *Atmos. Chem. Phys.*, 14, 3657–3690,
413 doi.org:10.5194/acp14-3657-2014, 2014.

414 Clough, S., Iacano, M. J. and Moncet, J.-L.: Line-by-line Calculations of Atmospheric Fluxes and Cooling Rates: Application
415 to Water Vapor. *J. Geophys. Res.* 97, 15761-15785, 1992.

416 Colarco, P., da Silva, A., Chin, M., and Diehl, T.: Online simulations of global aerosol distributions in the NASA GEOS-4
417 model and comparisons to satellite and ground-based aerosol optical depth, *J. Geophys. Res.*, 115, D14207,
418 doi:10.1029/2009JD012820, 2010.

419 Diaz, H. F., Carlson, T. N., and Prospero, J. M.: A study of the structure and dynamics of the Saharan air layer over the northern
420 equatorial Atlantic during BOMEX. National Hurricane and Experimental Meteorology Laboratory NOAA Tech. Memo.
421 ERL WMPO-32, 61 pp, 1976.

422 Diaz, J. P., Arbelo, M., Expósito, F.J., Podesta', G., Prospero, J.M., and Evans, R.: Relationship between errors in AVHRR-
423 derived sea surface temperature and the TOMS Aerosol Index, *Geophys. Res. Lett.*, 28, 1989 – 1992, 2001.

424 Divakarla, M., and Coauthors: Evaluation of CrIMSS operational products using in-situ measurements, model analysis fields,
425 and retrieval products from heritage algorithms, IEEE International Geoscience and Remote Sensing Symposium, Munich,
426 Germany, 2012, pp. 1046-1049, doi: 10.1109/IGARSS.2012.6350818, 2012.

427 Gelaro, R., McCarty, W., Suarez, M. J., Todling, R., and coauthors, 2017: The Modern-Era Retrospective Analysis for
428 Research and Applications, Version 2 (MERRA-2). *J. Climate*, 30, 5419–5454, doi.org: 10.1175/JCLI-D-16-0758.1, 2017.

429 Grogan, D., Lu, C.-H., Wei, S.-W., and Chen, S.-P.: Effects of Saharan dust on African easterly waves: The impact of aerosol-
430 affected satellite radiances on data assimilation, *Atmos. Chem. Phys. Disc.*, doi:10.5194/acp-2021-129, 2021.

431 Hale, G. M. and Querry, M. R.: Optical constants of water in the 200-nm to 200-mm wavelength region. *Appl. Opt.*, 12, 555–
432 563, 1973.

433 Han, Y., van Delst, P., Liu, Q., Weng, F., Yan, B., Treadon, R., and Derber, J.: JCSDA Community Radiative Transfer Model
434 (CRTM) – Version 1, NOAA NESDIS Tech. Rep. 122, 33 pp., NOAA, Silver Spring, Md, 2006.

435 Han, Y., Weng, F., Liu, Q., and van Delst, P.: A fast radiative transfer model for SSMIS upper atmosphere sounding channels.
436 *J. Geophys. Res.*, 112, D11121, doi:10.1029/2006JD008208, 2007.

437 Hess, M., Koepke, P., Schult I: Optical properties of aerosols and clouds: the software package 1528 OPAC. *Bull Am Met Soc*
438 79:831–844, 1998.

439 Highwood, E. J., Haywood, J. M., Silverstone, M. D., Newman, S. M., and Taylor, J. P.: Radiative properties and direct effect
440 of Saharan dust measured by the C-130 aircraft during Saharan Dust Experiment (SHADE): 2. Terrestrial spectrum, *J.*
441 *Geophys. Res.*, 108(D18), 8578, doi:10.1029/2002JD002552, 2003.

442 Karyampudi, V. M., Palm, S. P., Reagen, J. A., Fang, H., Grant, W. B., Hoff, R. M., Moulin, C., Pierce, H.
443 F., Torres, O., Browell, E. V., and Melfi, S. H.: Validation of the Saharan dust plume conceptual model using lidar,
444 Meteosat, and ECMWF data, *Bull. Am. Meteorol. Soc.*, 80, 1045–1075, doi:10.1175/1520-
445 0477(1999)080<1045:VOTSDP>2.0.CO;2.

446 Kim, J., Akella, S., da Silva, A.M., Todling, R., McCarty, W.: Preliminary evaluation of influence of aerosols on the simulation
447 of brightness temperature in the NASA's Goddard Earth Observing System Atmospheric Data Assimilation System; Tech.
448 Rep. Ser. Glob. Model. Data Assim., Vol 49, TM-2018-104606, Goddard Space Flight Center, National Aeronautics and
449 Space Administration: Greenbelt, Maryland, US, 2018.

450 Kleist, D. T., Parrish, D. F., Derber, J. C., Treadon, R., Wu, W. S., and Lord, S.: Introduction of the GSI into the NCEP Global
451 Data Assimilation System. *Weather and Forecasting*, 24(6):16911705, 2009.

452 Letertre-Danczak, J.: The Use of Geostationary Radiance Observations at ECMWF and Aerosol Detection for Hyper-Spectral
453 Infrared Sounders: 1st and 2nd Years Report; EUMETSAT/ECMWF Fellowship Programme Research Reports, Vol 40,
454 European Centre for Medium Range Weather Forecasts: Shinfield Park, Reading, RG2 9AX, England, 2016.

455 Liu, Q. and Weng, F.: Advanced doubling-adding method for radiative transfer in planetary atmosphere, *J. Atmos. Sci.*, 63,
456 3459-3465, doi:10.1175/JAS3808.1, 2006.

457 Liu, Q., Han, Y., van Delst, P., and Weng, F.: Modeling aerosol radiance for NCEP data assimilation, in *Fourier Transform
458 Spectroscopy/Hyperspectral Imaging and Sounding of the Environment*, paper HThA5, OSA Technical Digest Series,
459 Optical Society of America, doi:10.1364/HISE.2007.HThA5, 2007.

460 Liu, Q. and Lu, C.-H.: Community Radiative Transfer Model for Air Quality Studies. In *Light Scattering Reviews*. 456
461 Kokhanovsky, A., Eds.; Springer Praxis Books, Springer-Verlag, Berlin – Heidelberg, Germany, Volume 457, pp. 67-115,
462 2016.

463 Liu, Z., Liu, Q., Lin, H.-C., Schwartz, C. S., Lee, Y.-H., and Wang, T.: Three-dimensional variational assimilation of MODIS
464 aerosol optical depth: Implementation and application to a dust storm over East Asia, *J. Geophys. Res.*, 116, D23206,
465 doi:10.1029/2011JD016159, 2011.

466 Lu, C.-H., da Silva, A., Wang, J., Moorthi, S., Chin, M., Colarco, P., Tang, Y., Bhattacharjee, P. S., Chen, S.-P., Chuang, H.-
467 Y., Juang, H.-M. H., McQueen, J., and Iredell, M.: The implementation of NEMS GFS Aerosol Component (NGAC)
468 version 1.0 for global dust forecasting at NOAA/NCEP, *Geosci. Model Dev.*, 9, 1905–1919, doi: 10.5194/gmd-9-1905-
469 2016, 2016.

470 Matricardi, M.: The inclusion of aerosols and clouds in RTIASI, the ECMWF fast radiative transfer model for the infrared
471 atmospheric sounding interferometer, *ECMWF Tech. Memo.*, 474, doi: 10.21957/1krvb28ql, 2005.

472 Merchant, C. J., Embury, O., Le Borgne, P. and Bellec B.: Saharan dust in nighttime thermal imagery: Detection and
473 reduction of related biases in retrieved sea surface temperature, *Remote Sensing of Environ.*, 104, 15–30, doi:
474 10.1016/j.rse.2006.03.007, 2006.

475 Nalli, N. R., and L. L. Stowe, Aerosol correction for remotely sensed sea surface temperatures from the National Oceanic and
476 Atmospheric Administration advanced very high resolution radiometer, *J. Geophys. Res.*, 107(C10), 3172, doi:10.1029/
477 2001JC001162, 2002.

478 Pagowski, M., Liu, Z., Grell, G. A., Hu, M., Lin, H.-C., Schwartz, C. S., Implementation of aerosol assimilation in Gridpoint
479 Statistical Interpolation (v3.2) and WRF-Chem (v.3.4.1), *Geosci. Model Dev.*, 7, 1621–1627, doi:10.5194/gmd-7-1621-
480 2014, 2014.

481 Petty G: A First Course in Atmospheric Radiation, 2nd edition, Sundog Publishing, Madison, WI, 2006.

482 Peyridieu, S., Chdin, A., Tanr, D., Capelle, V., Pierangelo, C., Lamquin, N., and Armante, R.: Saharan dust infrared optical
483 depth and altitude retrieved from AIRS: a focus over North Atlantic comparison to MODIS and CALIPSO, *Atmos. Chem.*
484 *and Phys. Discuss.*, 9(5):2119921235, 2009.

485 Pierangelo, C., Chedin, A., Heilliette, S., Jacquinet-Husson, N., and R. Armante, R.: Dust altitude and infrared optical depth
486 from AIRS. *Atmos. Chem. Phys.*, 4, 1813-1822, doi: 10.5194/acp-4-1813-2004, 2004.

487 Randles, C. A., da Silva, A. M., Buchard, V., Colarco, P. R., Darmenov, A., Govindaraju, R., Smirnov, A., Holben, B., Ferrare,
488 R., Hair, J., Shinozuka, Y., Flynn, C., J: The MERRA-2 Aerosol Reanalysis, 1980 Onward. Part I: System Description and
489 Data Assimilation Evaluation, *Journal of Climate*, 30(17), 6823-6850, doi:10.1175/JCLI-D-16-0609.1, 2017.

490 Schwartz, C. S., Liu, Z., Lin, H.-C., and Cetola, J. D.: Assimilating aerosol observations with a “hybrid” variational-ensemble
491 data assimilation system, *J. Geophys. Res.-Atmos.*, 119, 4043–4069, doi:10.1002/2013JD020937, 2014.

492 Sokolik, I. N.: The spectral radiative signature of wind-blown mineral dust: Implications for remote sensing in the thermal IR
493 region: The spectral radiative signature of wind-blown mineral dust, *Geophys. Res. Lett.*, 29, 7-1-7-4,
494 doi:10.1029/2002GL015910, 2002.

495 Stegmann, P. G., Tang, G., Yang, P. and Johnson, B. T.: A stochastic model for density-dependent microwave Snow- and
496 Graupel scattering coefficients of the NOAA JCSDA community radiative transfer model, *J. Quant. Spec. Rad. Trans.*,
497 211, 9-24, doi:10.1016/j.jqsrt.2018.02.026, 2018.

498 Ukhov, A., Ahmadov, R., Grell, G., and Stenchikov, G.: Improving dust simulations in WRF-Chem model v4.1.3 coupled
499 with GOCART aerosol module, *Geosci. Model Dev. Disc.*, doi:10.5194/gmd-2020-92, 2021.

500 Wang, J., Bhattacharjee, P.S., Tallapragada, V., Lu, C.-H., Kondragunta, S., da Silva, A., Zhang, X., Chen, S.-P., Wei, S.-W.,
501 Darmenov, A.S., et al.: The implementation of NEMS GFS Aerosol Component (NGAC) Version 2.0 for global
502 multispecies forecasting at NOAA/NCEP – Part 1: Model descriptions., *Geosci. Model Dev.*, 11, 2315–2332,
503 doi:10.5194/gmd-11-2315-2018, 2018.

504 Weaver, C. J., Joiner, J., and Ginoux, P.: Mineral aerosol contamination of TIROS Operational Vertical Sounder (TOVS)
505 temperature and moisture retrievals., *J. Geophys. Res.*, 108, doi:10.1029/2002JD002571, 2003.

506 Wei, S.-W., Lu, C.-H., Liu, Q., Collard, A., Zhu, T., Grogan, D., Li, X., Wang, J., Grimbine, R., and Bhattacharjee, P.: The
507 impact of aerosols on satellite radiance data assimilation using NCEP global data assimilation system, *Atmos.*, 12(4), 432,
508 doi:10.3390/atmos12040432, 2021a.

509 Wei, S.-W., Lu, C.-H., Johnson, B. T., Dang, C., Stegmann, P., Grogan, D., Ge, G., and Hu, M.: The influence of aerosols on
510 satellite infrared radiance simulations and Jacobians: Numerical experiments of CRTM and GSI, *Remote. Sens.*, in review,
511 2021b.

512 Weng, F.: Advances in radiative transfer modeling in support of satellite data assimilation. *J. Atmos. Sci.*, 64, 3799–3807,
513 doi:10.1175/2007JAS2112.1, 2007.

514 Wu, W.-S., Purser, R. J., and Parrish, D. F.: Three-dimensional variational analysis with spatially inhomogeneous covariances,
515 *Mon. Weather Rev.*, 130, 2905–2916, doi:10.1175/1520-0493(2002)130<2905:TDVAWS>E2.0.CO;2, 2002.

516 Wu, M., Liu, X., Yu, H., Wang, H., Shi, Y., Yang, K., Darmenov, A., Wu, C., Wang, Z., Luo, T., Feng, Y., and Ke, Z.:
517 Understanding processes that control dust spatial distributions with global climate models and satellite observations,
518 *Atmos. Chem. Phys.*, 20, 13835–13855, <https://doi.org/10.5194/acp-20-13835-2020>, 2020.

519 Zhang L., Grell, G.A., Montuoro, R., McKeen, S. A., Bhattacharjee, P. S., Baker, B., Henderson, J., Pan, L., Frost, G. J.,
520 McQueen, J., Saylor, R., Ahmadov, R., Li, H., Wang, J., Stajner, I., Kondragunta, S., Zhang, X., Li, F.: Development of
521 GEFS-Aerosols into NOAAs Unified Forecast System UFS., *Geosci. Model Dev. Discuss.*, doi:10.5194/gmd-2021-378,
522 2021.